PRIFYSGOL ABERYSTWYTH UNIVERSITY

Aberystwyth University

Identification of Jupiter's magnetic equator through H3+ ionospheric emission

Stallard, Tom S.; Burrell, Angeline G.; Melin, Henrik; Fletcher, Leigh N.; Miller, Steve; Moore, Luke; O'Donoghue, James; Connerney, John E.P.; Satoh, Takehiko; Johnson, Rosie E.

Published in:
Nature Astronomy

DOI:
10.1038/s41550-018-0523-z

Publication date:
2018

Citation for published version (APA):
Stallard, T. S., Burrell, A. G., Melin, H., Fletcher, L. N., Miller, S., Moore, L., O'Donoghue, J., Connerney, J. E. P., Satoh, T., & Johnson, R. E. (2018). Identification of Jupiter's magnetic equator through H3+ ionospheric emission. *Nature Astronomy*, *2*(10), 773-777. https://doi.org/10.1038/s41550-018-0523-z

Document License
CC BY-NC

General rights
Copyright and moral rights for the publications made accessible in the Aberystwyth Research Portal (the Institutional Repository) are retained by the authors and/or other copyright owners and it is a condition of accessing publications that users recognise and abide by the legal requirements associated with these rights.

• Users may download and print one copy of any publication from the Aberystwyth Research Portal for the purpose of private study or research.
• You may not further distribute the material or use it for any profit-making activity or commercial gain
• You may freely distribute the URL identifying the publication in the Aberystwyth Research Portal

Take down policy
If you believe that this document breaches copyright please contact us providing details, and we will remove access to the work immediately and investigate your claim.

tel: +44 1970 62 2400
email: is@aber.ac.uk

Download date: 20. Mar. 2025

nature astronomy

SUPPLEMENTARY INFORMATION

https://doi.org/10.1038/s41550-018-0523-z

In the format provided by the authors and unedited.

Identification of Jupiter's magnetic equator through H_3^+ ionospheric emission

Tom S. Stallard[1]*, Angeline G. Burrell[1,2], Henrik Melin[1], Leigh N. Fletcher[1], Steve Miller[3], Luke Moore[4], James O'Donoghue[5], John E. P. Connerney[5,6], Takehiko Satoh[7] and Rosie E. Johnson[1]

[1]Department of Physics and Astronomy, University of Leicester, Leicester, UK. [2]Department of Physics, University of Texas at Dallas, Richardson, TX, USA. [3]Department of Physics and Astronomy, University College London, London, UK. [4]Center for Space Physics, Boston University, Boston, MA, USA. [5]Goddard Space Flight Center, NASA, Greenbelt, MD, USA. [6]Space Research Corporation, Annapolis, MD, USA. [7]Institute of Space and Astronautical Science, JAXA, Sagamihara, Japan. *e-mail: tss8@leicester.ac.uk

Supplementary information

Supplemental images to the materials and methods section.

Supplementary Figures 1-3 show the methods used to calibrate the data described within the materials and methods section.

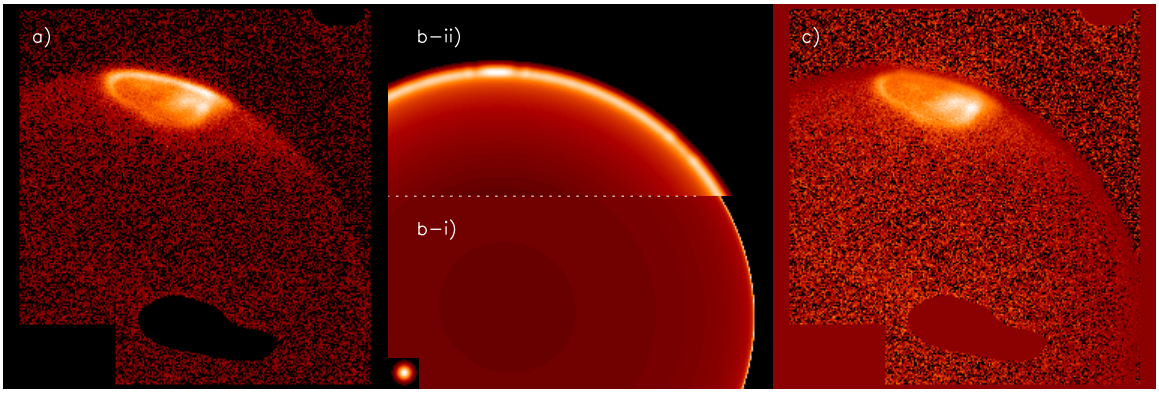

Supplementary Figure 1: An example image of H_3^+ emission (Panel-a), clearly showing line-of-sight enhancement along the limb. Here we show how the 'Line-of-sight correction to images' section of the Materials and Methods section corrects for this enhancement. Here, the image has already been processed to remove the 'ghost' emission (the black patches at the bottom of the image). A theoretical line-of-sight correction to each image is calculated by assuming a shell of H_3^+ emission between 400-500km (Panel b-1). This assumes a uniform illumination within the shell, to allow us to model the apparent line-of-sight enhancement for a given viewing angle and atmospheric turbulence in Earth's atmosphere. To account for atmospheric turbulence, we smooth out the theoretical emission by applying a 2D convolution using a Gaussian with a FWHM that models the 'seeing' measured from the star calibration images from that night (shown at the bottom of Panel b-1). This results in a smoothed line-of-sight enhancement (Panel b-

ii) which emulates the line-of-sight enhancement in the actual image. This matches well, especially away from the auroral region, where the H_3^+ is largely generated by uniform EUV ionization. We can then use this to convert line-of-sight enhanced brightness into a column-integrated brightness that can then be mapped into latitude and longitude co-ordinates. The original image is divided by the seeing-smoothed modelled line-of-sight enhancement (where this enhancement is normalised to 1 at the equator), resulting in an image of column intensity (Panel-c) that can then be mapped.

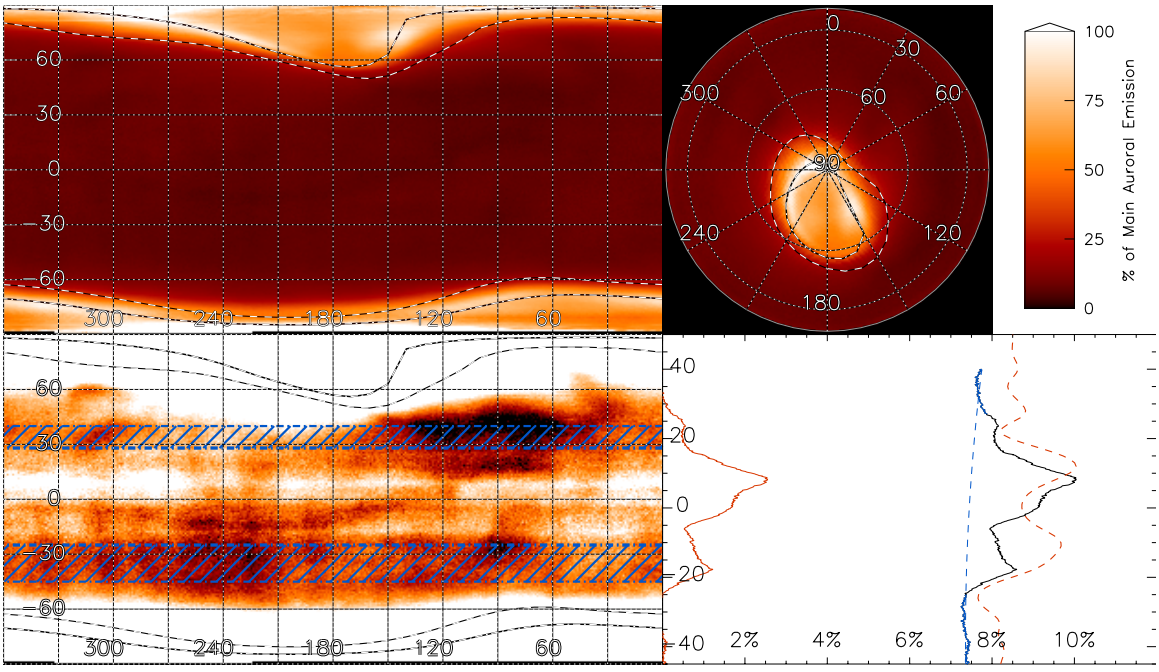

Supplementary Figure 2: Observed emission from Jupiter. The top-left panel shows a cylindrical map of the square root of the observed emission (left) scaled between zero and MAB, with the longitude measured in degrees West. All emission is scaled with reference to the main auroral brightness (MAB) measured between 75˚N and 75˚S. The location of the main auroral emission (black and white dot-dashed line) and Io spot and

trail (black and white dashed line) are taken from the Grodent et al (2008) model. The top-right panel shows a northern polar orthographic projection of this map, clearly showing the average H_3^+ auroral emission across this dataset. The bottom-left panel shows a cylindrical map of the same data, here scaled between 6% and 10% of MAB, revealing emission in the equatorial region which is clearly dominated by two bands of tropospheric emission that extend across all longitudes, centred on 8˚N and 18˚S. Away from these tropospheric peaks, we have highlighted two mid-latitude bands used to calculate the background intensity (blue diagonal area). The bottom-right panel shows the mean emission across all longitudes (black line), along with a typical tropospheric intensity profile, measured at 5.38 microns (red dashed line). To remove this tropospheric emission, we fit a background intensity from the mid-latitude region (blue dashed line fitted to blue data), and subtract this, resulting in a measure of the average tropospheric brightness with latitude (red solid line).

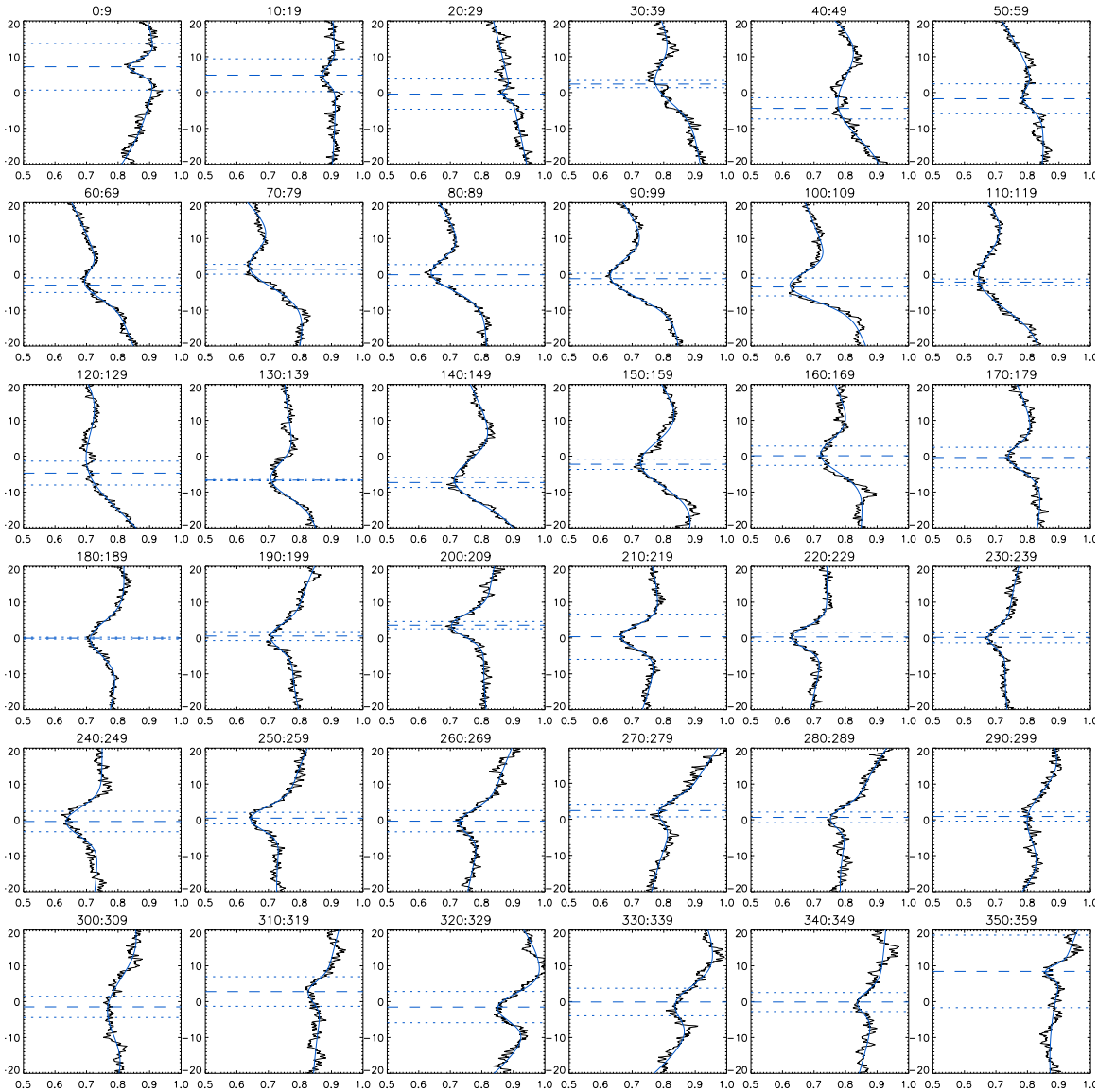

Supplementary Figure 3: The individual plots of emission between 20N and 20S, binned into 10 degrees longitude bins (black solid line). This data was then fitted with a Gaussian with a quadratic background (blue thin line), the peak of which is denoted (dotted lines). The minimum value within each profile was also found (dashed line). The values used are bolded and shown in red.

Testing the ghost removal technique from Stallard et al., 2017

Although we have previously utilized a technique of removing parts of the image affected by internally-reflected light in the instrument in Stallard et al., 2017, the application of this method in the equatorial region means that we found it prudent to test whether this removal technique was artificially producing the changes observed in ionospheric brightness.

Two tests were performed. Firstly, we significantly broadened the region covered by the ghost mask to include the reflected region from a broad area of the auroral limb, re-running the measured equatorial emission with this larger region removed from the data. This effectively removes the mirrored light from the entire polar limb regions, rather than just the region that is brightest – the ghosting removal for other bright features (like the moons) remained the same, as these are relatively infrequent. An example of one image with this mask removed is given in Supplementary Figure 4. Using this broader removal results in a noisier view of the equator, since we have removed more of the equatorial light, as shown in Supplementary Figure 5, a new version of Figure 1 from the paper. Despite removing a more signal from each image, the same ionospheric features appear, including the dark ribbon, and the dark spots close to 90°W. This strongly suggests that the ionospheric features are not affected by the ghosting, or its removal.

The second test, designed to ensure ghosting does not affect our results, uses a synthetic image with a calculated ghost effect. The advantage of this technique is that we can set

74 the equatorial emission to be uniform, so that we can directly assess the resultant effect of
75 the ghost removal technique. This technique runs through the entire dataset, creating a
76 synthetic image for every real image in the dataset. For each image, we take the cml, sub-
77 earth latitude, center of planet, planet width, seeing and ghost rotation/offset for that
78 particular image and re-create the image using a modelled H_3^+ emission map. This map is
79 the average intensity map shown in Figure 1 of the paper, but with the non-auroral
80 regions (40˚N to 40˚S) set to a constant value. We then add tropospheric emission and
81 add line-of-sight brightening. To emulate the effect of turbulence in the Earth's
82 atmosphere, we convolve the image by a point-spread function with a full-width half-
83 maximum taken from the seeing measured on that night. We then calculate a ghost
84 image. The degree of ghosting seems to vary significantly between different images,
85 with some stellar images showing ghosts as high as ~1/15 brightness. Although this is
86 much higher than most images, we want to test to the extremes of the possible ghosting,
87 so we use this higher value as an end point (the weaker the ghost, the lower the effects we
88 expect in correcting for it).
89
90 Supplementary Figure 4 shows an example of the synthetic data before and after the
91 ghosting mask has been removed. We use the enlarged mask shown early in this section,
92 to provide a direct comparison. The aurora is more diffuse in the synthetic image, since
93 the averaging process has smoothed the mean auroral brightness somewhat, and the
94 ghost is clearly weaker in the real image than the synthetic image, but otherwise, we have
95 emulated the real image in an effective way. As a result, we can then insert this synthetic

image back into the same mapping process as was used in the paper, and compare and contrast the resultant ionospheric map.

The synthetic ionospheric map is shown in Supplementary Figure 6. This shows that there is no significant correspondence between the modelled emission structure and the ghosting. The poorly removed ghost outside of the mask has affected the apparent brightness of the synthetic ionosphere (which should be uniform) with regions of brightening and darkening not matching variability in the real data, as shown in Supplementary Figure 5, in particular, with no dark features aligning with either the dark ribbon or any of the dark features at 90W. The profile that follows the location of the dark ribbon shows no trough at the center. In conclusion, even applying an overly-strong ghost effect does not replicate any feature seen in the H_3^+ brightness map. As such, there is no evidence that the ghosting, and the techniques used to remove them, significantly affect the measured H_3^+ brightness map.

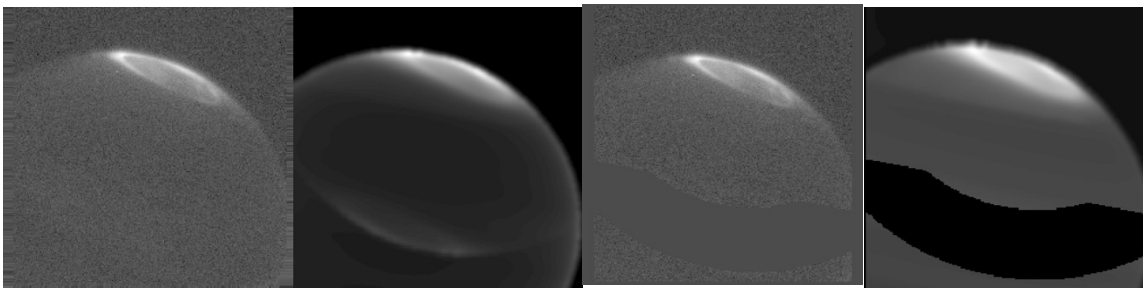

Supplementary Figure 4: An example H_3^+ image from 18 December 2000. In the left panel, the auroral oval and the planetary limb can be seen clearly, but the 'ghosting' feature is very weak. The second panel shows our synthetic image, produced by projecting the average auroral emission at the planetary orientation, enhanced by the line-

of-sight effects, convolved by the seeing observed on that night then inversed to produce a model of the 'ghosting' – here the ghost is at 1/10th brightness, the strongest ghost features observed within the entire dataset, though clearly much brighter than the 'ghost' present in this image. The third panel shows the real image with the larger ghost-filter, which removes all the light from the polar region. The fourth panel shows this same filter on the synthetic image.

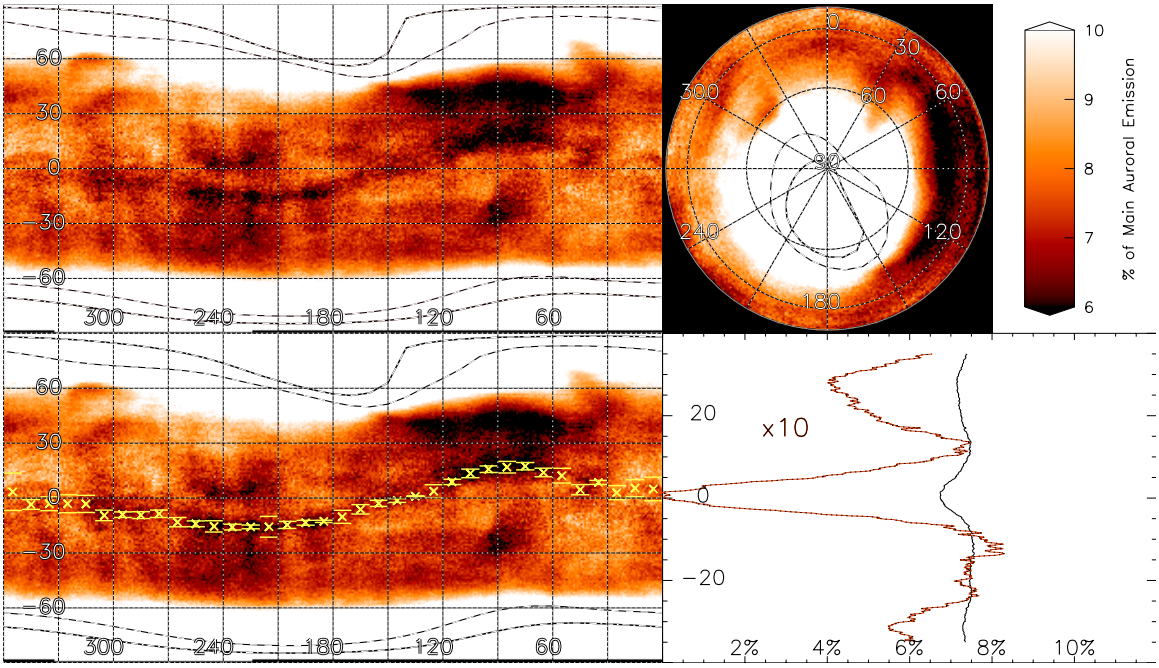

Supplementary Figure 5: The measured ionospheric emission observed using the enlarged ghost filter, a duplicate of Figure 1 of the paper with these new values.

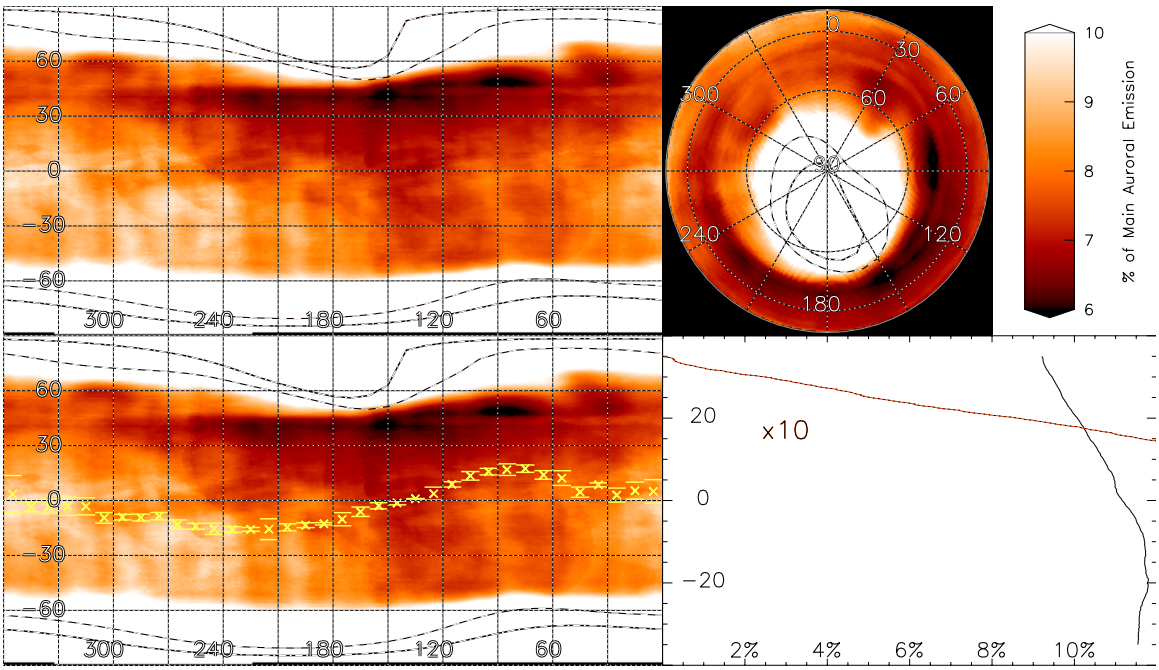

Supplementary Figure 6: The synthetic ionospheric brightness with the enlarged ghost filter. Here, the synthetic equator is uniform between 40N and 40S, so this region shows the variations expected as an artefact of the removal of the ghost. This can be directly compared with Supplementary Figure 2.

Detection of equatorial features in individual filters

In order to ensure the features seen in the equatorial regions are not the result of values coming from individual filters, we have produced three additional maps using three sub-sets of the images. It was necessary to apply a full line-of-sight correction to the data to ensure the accuracy of the measurements of the equatorial features described in this paper, it was necessary to apply a full line-of-sight correction to the data. However, H_3^+ is strongly limb-brightened, while the background signal of underlying tropospheric absorbing is weakened by stratospheric methane, so that it is limb-darkened. As such, applying a line-of-sight correction significantly decreases the signal/noise of the

observation. In order to provide as strong a signal as possible, when analyzing sub-sets of filters, we do not apply the line-of-sight correction to these images. This means that the equator to pole gradient for each map is incorrect, but results in a much higher overall signal-to-noise.

In Supplementary Figures 7-9, we show the dark ribbon feature using three filter subsets. Supplementary Figures 7-8 both use individual images taken with individual Connerney H_3^+ filters focused on 3.4265 micron and 3.5420 microns respectively. In these narrow filters, the equatorial features are clearly observed. In Supplementary Figure 9, we combine images that use the 3.420, 3.430 and 3.460 micron filters. Here, neither the H_3^+ equatorial emission or the background tropospheric emission is nearly as clearly distinct. The data is shown summed across all longitudes following latitudinal position of the equatorial equator (bottom right panel), revealing a slight dip is seen directly on the equator, but the strength of the decrease is significantly less than in the narrower Connerney filters. This apparent reduction in the strength of the equatorial features is likely to be the result of the broader filter width resulting in a much lower signal to noise, given the similar weakening of tropospheric emission. However, it is possible that this results from the change of season from southern summer during the early observations using these filters (~1995-1997) and northern summer, when the Connerney filters were used (~1998-2000).

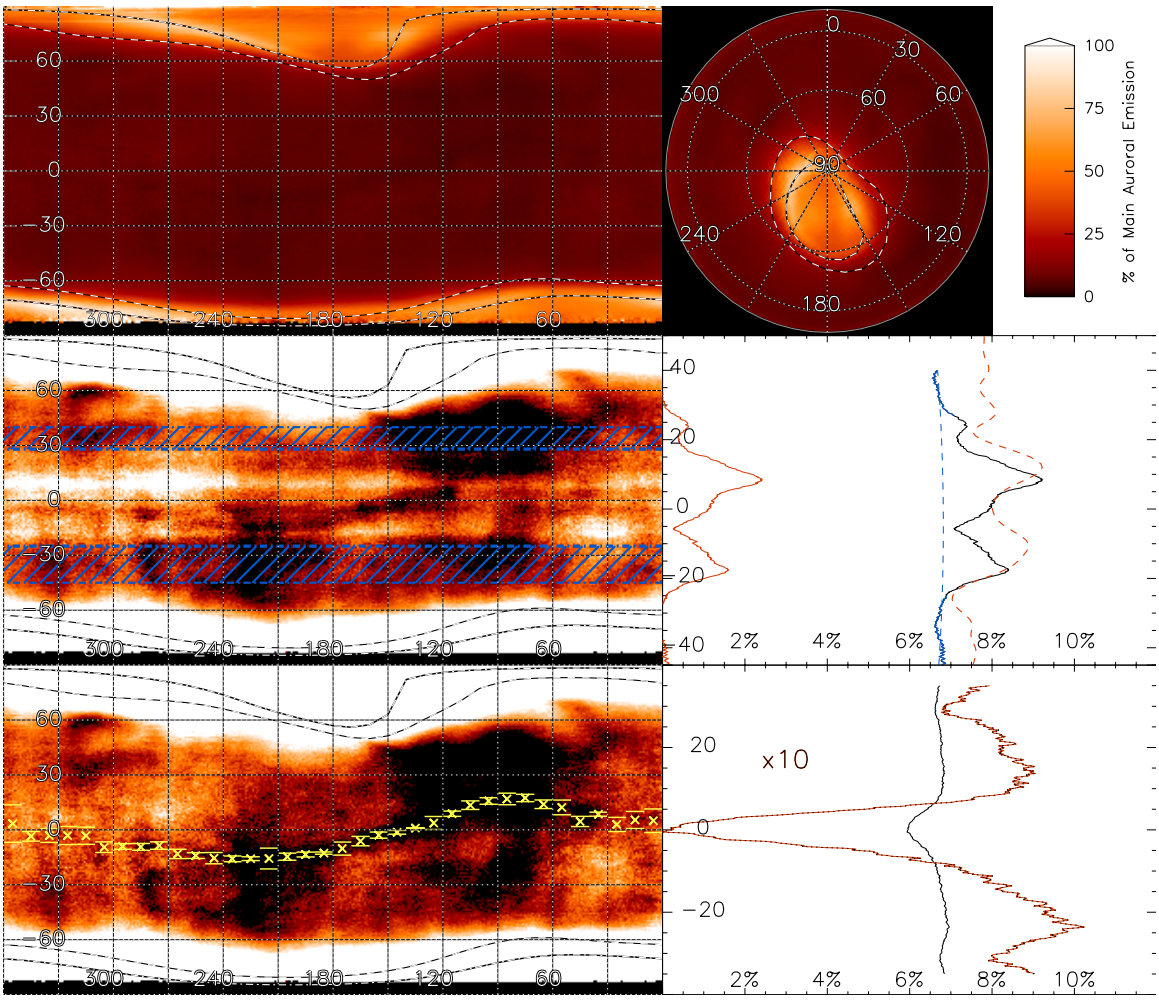

Supplementary Figure 7: A version of Figure 1 in the paper and Supplementary Figure 2 referenced in the Materials and Methods section and shown above, here using only images taken with the 3.4265 micron filter. Middle and bottom maps range between 6%-10%, as with Figs 1 and S2.

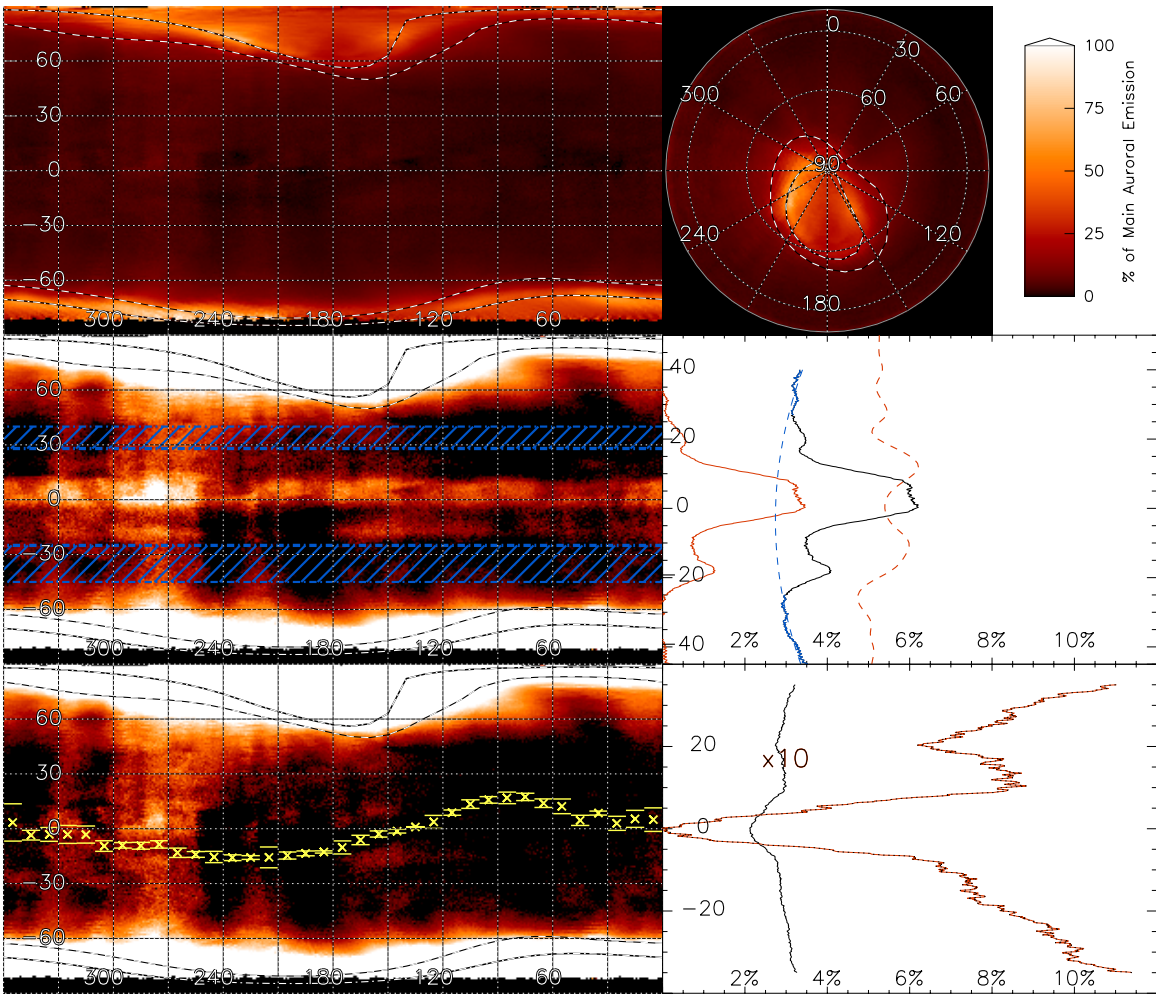

Supplementary Figure 8: A version of Figure 1 in the paper and Supplementary Figure 2 referenced in the Materials and Methods section and shown above, here using only images taken with the 3.5420 micron filter. Note, the brightness here is lower, so the maps in the middle and bottom panels are shown with a range of 3%-10%.

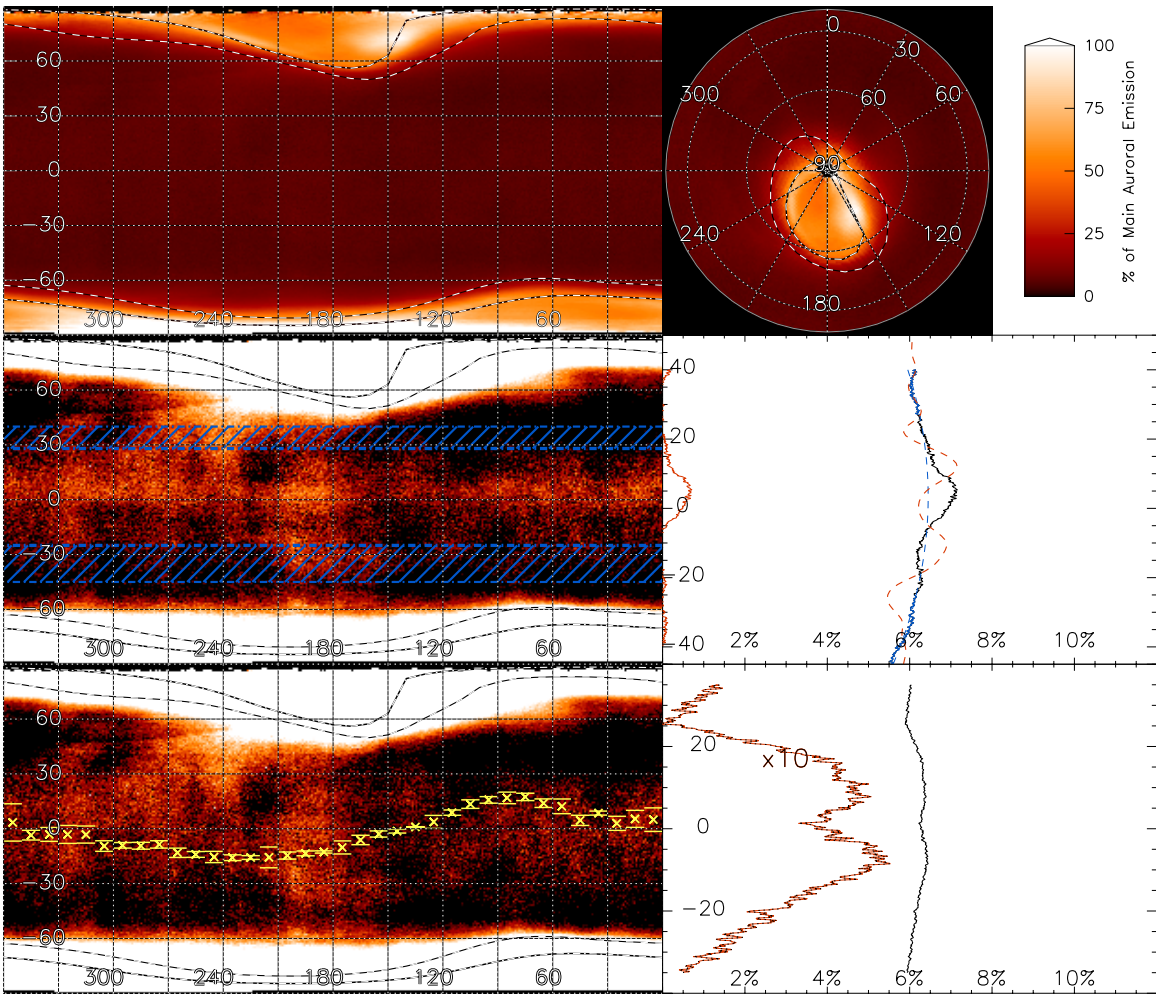

Supplementary Figure 9: A version of Figure 1 in the paper and Supplementary Figure 2 referenced in the Materials and Methods section and shown above, here using only images taken with the 3.420, 3.430 and 3.460 micron filters. Middle and bottom maps range between 6%-10%, as with Figs 1 and S2.

Rayner, J. T., Cushing, M. C., Vacca, W. D. (2009), The Infrared Telescope Facility (IRTF) Spectral Library: Cool Stars, The Astrophysical Journal Supplement Series 185, 289-432, DOI:10.1088/0067-0049/185/2/289